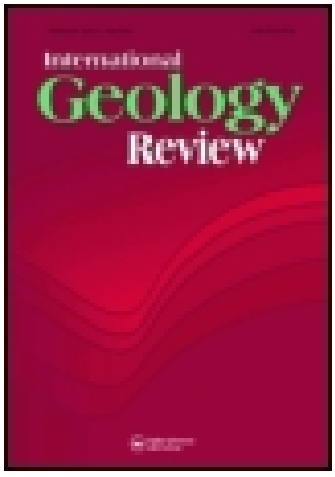
This article was downloaded by: [USGS Libraries]
On: 18 February 2015, At: 12:06
Publisher: Taylor & Francis
Informa Ltd Registered in England and Wales Registered Number: 1072954 Registered office: Mortimer House, 37-41 Mortimer Street, London W1T 3JH, UK



CrossMark
Click for updates

International Geology Review
Publication details, including instructions for authors and subscription information:
http://www.tandfonline.com/loi/tigr20

High influx of carbon in walls of agglutinated foraminifers during the Permian-Triassic transition in global oceans

Galina P. Nestell[a], Merlynd K. Nestell[a], Brooks B. Ellwood[b], Bruce R. Wardlaw[c], Asish R. Basu[a], Nilotpal Ghosh[ad], Luu Thi Phuong Lan[e], Harry D. Rowe[f], Andrew Hunt[a], Jonathan H. Tomkin[g] & Kenneth T. Ratcliffe[h]

[a] Department of Earth and Environmental Sciences, University of Texas at Arlington, Arlington, USA

[b] Department of Geology and Geophysics, Louisiana State University, Baton Rouge, USA

[c] Eastern Geology and Palaeoclimate Science Center, United States Geological Survey, Reston, USA

[d] Department of Earth and Environmental Sciences, University of Rochester, Rochester, USA

[e] Department of Geomagnetism, Institute of Geophysics, Vietnamese Academy of Science and Technology, Hanoi, Vietnam

[f] Bureau of Economic Geology, University of Texas at Austin, University Station, Austin, USA

[g] School of Earth, Society, and Environment, University of Illinois, Urbana, USA

[h] Chemostrat Inc, Houston, USA

Published online: 16 Feb 2015.

To cite this article: Galina P. Nestell, Merlynd K. Nestell, Brooks B. Ellwood, Bruce R. Wardlaw, Asish R. Basu, Nilotpal Ghosh, Luu Thi Phuong Lan, Harry D. Rowe, Andrew Hunt, Jonathan H. Tomkin & Kenneth T. Ratcliffe (2015): High influx of carbon in walls of agglutinated foraminifers during the Permian-Triassic transition in global oceans, International Geology Review, DOI: 10.1080/00206814.2015.1010610

To link to this article: http://dx.doi.org/10.1080/00206814.2015.1010610

PLEASE SCROLL DOWN FOR ARTICLE

Taylor & Francis makes every effort to ensure the accuracy of all the information (the "Content") contained in the publications on our platform. However, Taylor & Francis, our agents, and our licensors make no representations or warranties whatsoever as to the accuracy, completeness, or suitability for any purpose of the Content. Any opinions and views expressed in this publication are the opinions and views of the authors, and are not the views of or endorsed by Taylor & Francis. The accuracy of the Content should not be relied upon and should be independently verified with primary sources of information. Taylor and Francis shall not be liable for any losses, actions, claims, proceedings, demands, costs, expenses, damages, and other liabilities whatsoever or howsoever caused arising directly or indirectly in connection with, in relation to or arising out of the use of the Content.

This article may be used for research, teaching, and private study purposes. Any substantial or systematic reproduction, redistribution, reselling, loan, sub-licensing, systematic supply, or distribution in any form to anyone is expressly forbidden. Terms & Conditions of access and use can be found at http://www.tandfonline.com/page/terms-and-conditions

International Geology Review, 2015
http://dx.doi.org/10.1080/00206814.2015.1010610

Taylor & Francis
Taylor & Francis Group

High influx of carbon in walls of agglutinated foraminifers during the Permian–Triassic transition in global oceans

Galina P. Nestell[a]*, Merlynd K. Nestell[a], Brooks B. Ellwood[b], Bruce R. Wardlaw[c], Asish R. Basu[a], Nilotpal Ghosh[a,d], Luu Thi Phuong Lan[e], Harry D. Rowe[f], Andrew Hunt[a], Jonathan H. Tomkin[g] and Kenneth T. Ratcliffe[h]

[a]*Department of Earth and Environmental Sciences, University of Texas at Arlington, Arlington, USA;* [b]*Department of Geology and Geophysics, Louisiana State University, Baton Rouge, USA;* [c]*Eastern Geology and Palaeoclimate Science Center, United States Geological Survey, Reston, USA;* [d]*Department of Earth and Environmental Sciences, University of Rochester, Rochester, USA;* [e]*Department of Geomagnetism, Institute of Geophysics, Vietnamese Academy of Science and Technology, Hanoi, Vietnam;* [f]*Bureau of Economic Geology, University of Texas at Austin, University Station, Austin, USA;* [g]*School of Earth, Society, and Environment, University of Illinois, Urbana, USA;* [h]*Chemostrat Inc, Houston, USA*

(*Received 3 July 2014; accepted 16 January 2015*)

The Permian–Triassic mass extinction is postulated to be related to the rapid volcanism that produced the Siberian flood basalt (Traps). Unrelated volcanic eruptions producing several episodes of ash falls synchronous with the Siberian Traps are found in South China and Australia. Such regional eruptions could have caused wildfires, burning of coal deposits, and the dispersion of coal fly ash. These eruptions introduced a major influx of carbon into the atmosphere and oceans that can be recognized in the wall structure of foraminiferal tests present in survival populations in the boundary interval strata. Analysis of free specimens of foraminifers recovered from residues of conodont samples taken at a Permian–Triassic boundary section at Lung Cam in northern Vietnam has revealed the presence of a significant amount of elemental carbon, along with oxygen and silica, in their test wall structure, but an absence of calcium carbonate. These foraminifers, identified as *Rectocornuspira kalhori*, *Cornuspira mahajeri*, and *Earlandia* spp. and whose tests previously were considered to be calcareous, are confirmed to be agglutinated, and are now referred to as *Ammodiscus kalhori* and *Hyperammina deformis*. Measurement of the $^{207}Pb/^{204}Pb$ ratios in pyrite clusters attached to the foraminiferal tests confirmed that these tests inherited the Pb in their outer layer from carbon-contaminated seawater. We conclude that the source of the carbon could have been either global coal fly ash or forest fire-dispersed carbon, or a combination of both, that was dispersed into the Palaeo-Tethys Ocean immediately after the end-Permian extinction event.

Keywords: foraminifers; carbon; lead isotopes; pyrite clusters; Permian–Triassic transition; Vietnam

Downloaded by [USGS Libraries] at 12:06 18 February 2015

1. Introduction

One of the greatest mass extinctions during the history of life on Earth occurred at the Palaeozoic and Mesozoic boundary. This extinction event was more severe than the one related to the demise of dinosaurs at the Mesozoic–Cenozoic boundary. More than 90% of terrestrial and marine species became extinct near the Permian–Triassic boundary (PTB) (Raup 1979; Hallam and Wignall 1997). In marine biota, the extinction affected tabulate and rugose corals, several classes of echinoderms and also some groups of ostracodes, brachiopods, bryozoans, bivalves, ammonoids, nautiloids, radiolarians, acritarchs, and foraminifers (Hallam and Wignall 1997). The cause, or causes, of this severe biotic extinction event has long been sought, together with the determination of whether it was gradual, stepped, or abrupt. To try to answer these questions, many stratigraphic sections spanning the PTB have been studied using palaeontological, lithological, magnetostratigraphic, and geochemical methods. After the formal designation of the Permian–Triassic GSSP (Global Boundary Stratotype Section and Point) was made at Meishan, China, based on the first occurrence of the conodont *Hindeodus parvus* (Yin *et al.* 2001), many PTB sections have been reinvestigated using this criterion. Furthermore, several hypotheses have been proposed that suggest that multiple interrelated mechanisms caused the Permian–Triassic extinction. One of the more controversial proposals is that an extraterrestrial impact (Becker *et al.* 2001; Kaiho *et al.* 2001; Basu *et al.* 2003) could have triggered the rapid volcanism that produced the extensive Siberian flood basalt known as the Siberian Traps (Renne and Basu 1991; Renne *et al.* 1995; Kamo *et al.* 2003; Korte *et al.* 2010). This event could, in turn, have led to an enhanced production of carbon dioxide (Hallam and Wignall 1997; Brand *et al.* 2012), a climatic warming (Hallam and Wignall 1997; Kidder and Worsley 2004; Joachimski *et al.* 2012), a change in ocean chemistry to more anoxic conditions (Wignall and Twitchett 1996; Isozaki 1997), a significant disturbance of the carbon cycle (Berner 2002), a change in ocean salinity (Kidder and Worsley 2004), a large shift in the composition of sulphur

*Corresponding author. Email: gnestell@uta.edu

© 2015 Taylor & Francis

Downloaded by [USGS Libraries] at 12:06 18 February 2015

and strontium isotopes (Newton *et al.* 2004; Riccardi *et al.* 2006; Algeo *et al.* 2008; Kaiho *et al.* 2012), and a denitrification of the water mass (Knies *et al.* 2013). Drops in atmospheric oxygen (Weidlich *et al.* 2003) and sea level have also been suggested (Hallam and Wignall 1999; Wu *et al.* 2010). The extensive volcanism in the northern hemisphere resulting in the accumulation of the Siberian Traps may have led to the combustion of late Permian coal deposits and the dispersion of coal fly ash into the oceans (Grasby *et al.* 2011; Ogden and Sleep 2012). Recently, evidence of unrelated volcanic eruptions producing several episodes of ash falls synchronous to the Siberian flood basalt has been found in South China (J. Shen *et al.* 2013). Such regional eruptions could have caused wildfires on land, and the products of combustion could have been buried on land, as well as dispersed in the ocean (Shen *et al.* 2011b). Traces of such a wildfire in the late Permian have been found in the Perth basin of Western Australia (Thomas *et al.* 2004). These eruptions could have introduced major amounts of carbon into the atmosphere and global oceans. A combination of all of these factors, leading to environmental and biotic changes, could have contributed to the Permian–Triassic mass extinction.

The main purpose of this paper is to document a large influx of carbon from volcanic-induced events into the marine environment in latest Permian time and to propose that this influx was part of the extinction and slow recovery process. The carbon particles can be recognized in the wall structure of agglutinated foraminiferal tests of survival taxa in the boundary interval strata. In order to establish a foundation for interpreting the carbon influx, we present the stratigraphic setting of the PTB sequence in the Lung Cam section in Vietnam, lead (Pb) isotopic data from pyrite grains attached to the foraminiferal tests, carbon isotopic data from the samples, and a time-series analysis of magnetic susceptibility data from the stratigraphic sequence.

2. Geological and stratigraphic setting

We focus on a section of the PTB interval located in northern Vietnam in the Lung Cam region of Ha Giang Province (Figure 1).

2.1. *Previous work on the Lung Cam section*

The Lung Cam section was previously studied by Son *et al.* (2007), together with the Nhi Tao section (also studied by Algeo *et al.* 2007), farther to the east in Vietnam. Their work was an attempt to define the precise level of the PTB in these Vietnamese sections and to document the carbon and oxygen isotopic content, trace element variations, and other global perturbations associated with the PTB. The authors did not report the presence of any conodonts in the boundary interval, and they placed the PTB based solely on the change of lithology and fossil content. One specimen of *H. parvus* was found in Nhi Tao bed 20, but the authors argued that this occurrence was well above the boundary (Algeo *et al.* 2007). Son *et al.* (2007) reported that limestone of the Dong

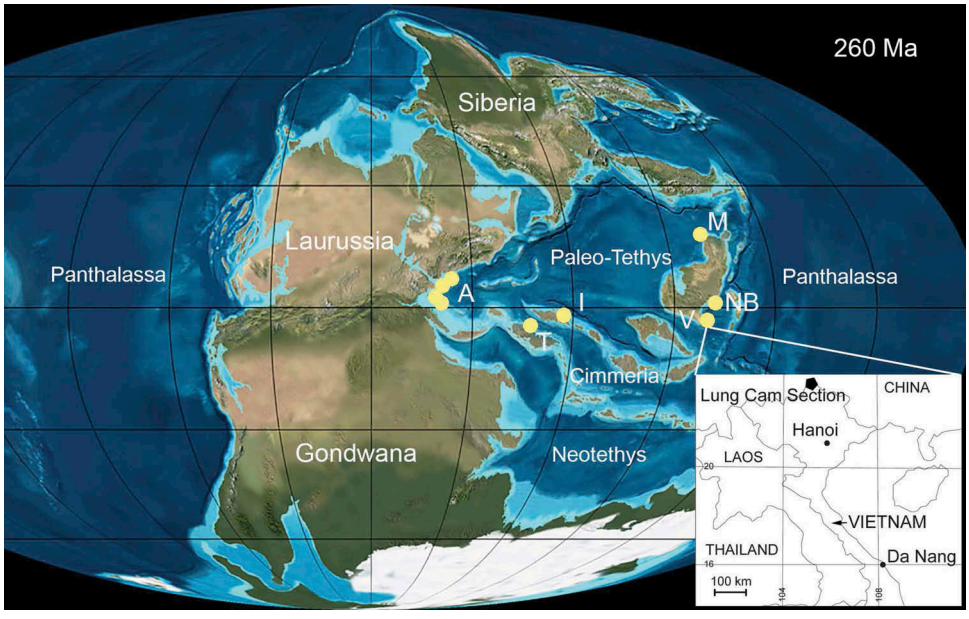


Figure 1. The distribution of species of *Ammodiscus kalhori* (Brönnimann, Zaninetti, and Bozorgnia) and *Hyperammina deformis* (Bérczi-Makk) in the Palaeo-Tethys Ocean in the late Permian (after Blakey 2003), and the location map of the Lung Cam section in northern Vietnam. (A) Hungary, Austria, Slovenia and Italy; (T) Turkey; (I) northern Iran; (V) northern Vietnam, Lung Cam section; (NB, M) South China: NB, Nanpanjiang Basin; M, Meishan section, GSSP for the Permian–Triassic boundary.

Downloaded by [USGS Libraries] at 12:06 18 February 2015

Dang Formation with typical and abundant Changhsingian foraminifers, including fusulinaceans, changes to dolomitic limestone of the Hong Ngai Formation with rare foraminifers of the genera *Ammodiscus* and *Globivalvulina*. In the Lung Cam section, the PTB was placed at the top of a shale layer (bed T 830/5 in Figure 4 in Son *et al.* 2007, p. 58). This boundary is defined on lithology, coinciding with an environmental change (a palaeoecological boundary), but is not a chronostratigraphic boundary. Moreover, Son *et al.* (2007) stopped their study of the section about 70 cm above their PTB level (total section thickness 2.2 m).

2.2. *Biostratigraphy of the Lung Cam section*

Recently, the Lung Cam section has been carefully sampled by Ellwood and Luu Thi Phuong Lan (and resampled several times) and studied using palaeontological, lithological, magnetic susceptibility, and geochemical methods. The total PTB section studied is ~21 m thick, with the focus in this paper on an approximately ~4 m-thick interval that contains enough fossil evidence, including many specimens of *H. parvus*, to define the PTB. The interval discussed herein consists (in ascending order) of (1) approximately 1 m of limestone (beds 5–11), (2) a very thin microbial limestone layer (bed 12) and (3) a 14 cm-thick layer of ash tuff (bed 13, which corresponds to the shale bed T 830/5 of Son *et al.* 2007), which is correlated to bed 25 at the Meishan GSSP section (Yin *et al.* 2001). This ash bed is overlain by a 2.3 m-thick unit of siderite and/or ankerite limestone (beds 14–32) (Figure 2). The lithology of the lower part of this unit has been described as a dolomitic limestone by Son *et al.* (2007). However, XRD analyses and Mg/Ca ratios of most samples throughout the Lung Cam section do not indicate any significant dolomite. The misinterpretation in this regard by Son *et al.* (2007) is probably due to the presence of siderite/ankerite rhombs, commonly mistaken for dolomite. Throughout the section, there are a number of thin volcanic ash beds with bed 13 being one of the thickest (Figure 2). XRD results for samples from bed 13 show mainly quartz, mica and feldspar.

Free specimens of foraminifers and microconchids have been recovered (for the first time from any PTB section) in the Lung Cam section. Some of these specimens are shown in Figure 3 (e–g, l–o, q, s, u, v), along with their thin-section views (Figure 3a–d, h–k). The same types of taxa can be seen in thin sections from other PTB sections in the Palaeo-Tethys area: northern Iran

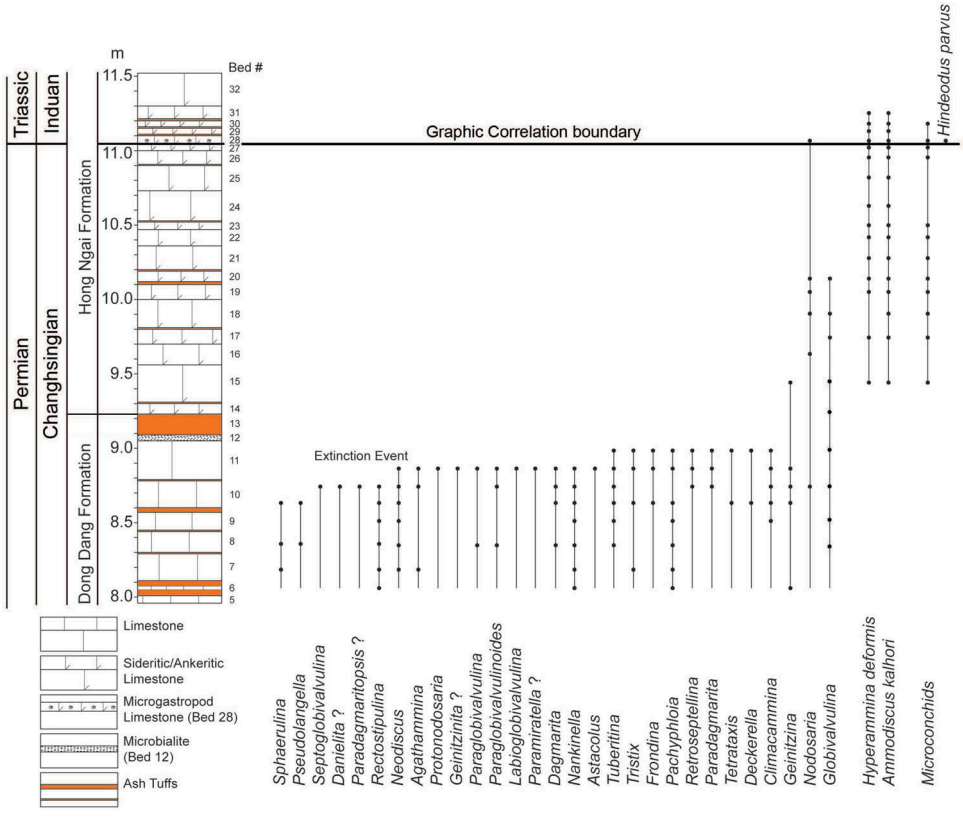


Figure 2. Stratigraphic column of the Lung Cam section with the distribution of the foraminiferal genera and species, microconchids, and the conodont *Hindeodus parvus*. Beds 10 and 11 are considered an event horizon with stepped extinction.

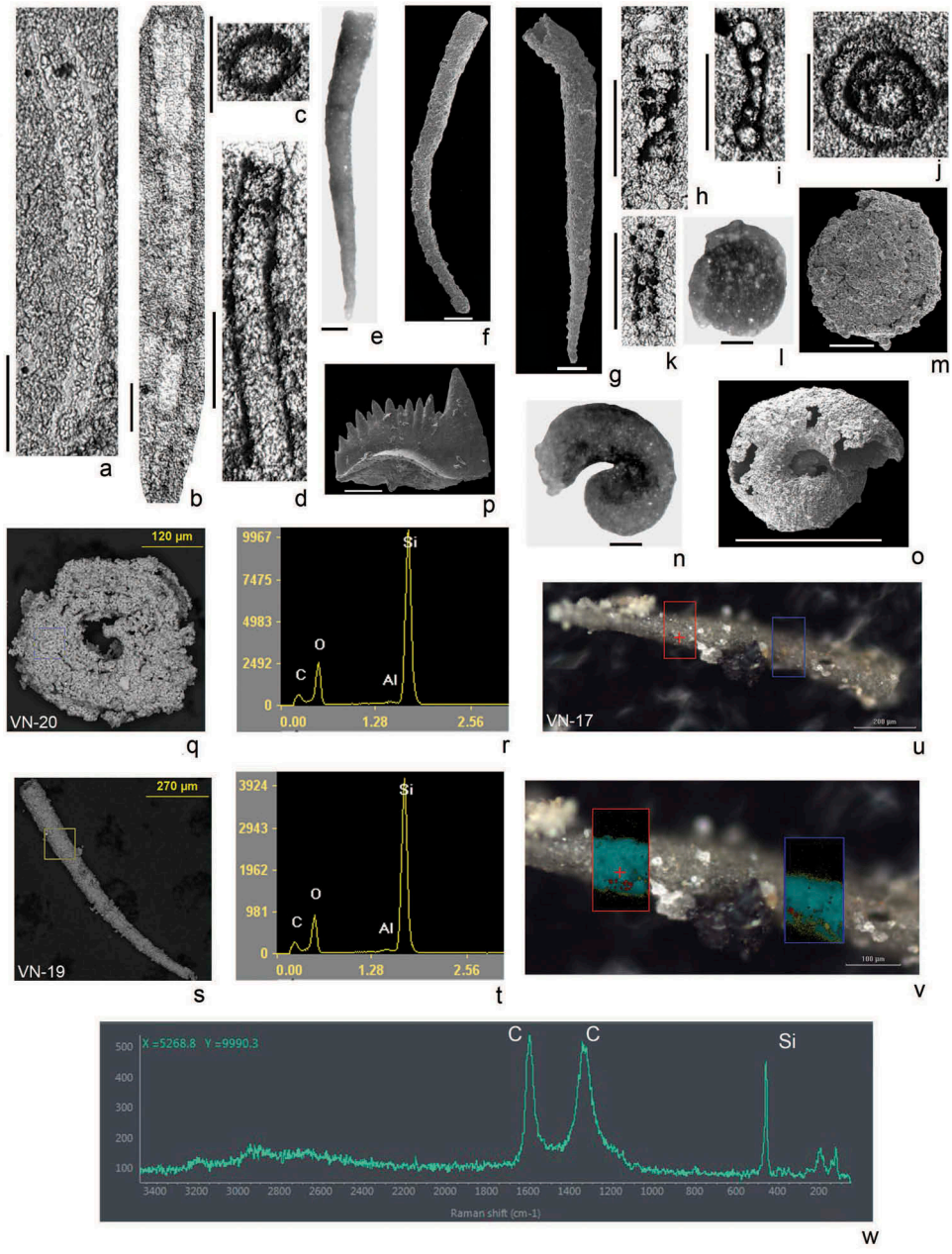


Figure 3. Representatives of the species *Hyperammina deformis* (Bérczi-Makk) (a–d in thin sections; e–g, free specimens), *Ammodiscus kalhori* (Brönnimann, Zaninetti, and Bozorgnia) (h–k in thin sections; l–m, free specimens), *Microconchus phlyctaena* (Brönnimann and Zaninetti) (o), *M*. sp. (n), and *Hindeodus parvus* (Kozur and Pjatakova) (p). Significant darkening of the walls due to the presence of carbon can be clearly seen in (b–d) and (h–k) and on the exterior of the free specimens in (e, l, n). The specimen shown in (a) has only an agglutinated siliceous wall and there is no indication of the presence of black carbon. However, there is still carbon present that can be detected by the EDX (q, r and s–t). (q) Backscattered electron image and (r) energy-dispersive X-ray spectrum from the selected area (scan box) of *A. kalhori*. (s) Backscattered electron image and (t) energy-dispersive X-ray spectrum from points in selected area (scan box) of *H. deformis*. (u) Image of *H. deformis* taken with a 'DXR'xi Raman imaging microscope, with boxes indicating where the test was analysed, (v) enlarged image of (u), and (w) Raman spectral composition of the points marked with a red cross on (u) and (v). The spectrum indicates the presence of both C and Si in the foraminiferal test. (a) Sample LC-23; (b, h, k, n) sample VN-21; (c, d, i, j) sample VN-15; (e, g) sample VN-18; (f, l, m) sample VN-20; (o) sample VN-23; (p) sample LC-28. Scale bar 100 µm, except (o) 1 mm.

(Brönnimann *et al.* 1972); northern Hungary (Bérczi-Makk 1987); Great Bank of Guizhou, Nanpanjiang Basin, South China (Song *et al.* 2009); Southern Alps, northern Italy (Groves *et al.* 2007); western Slovenia (Nestell *et al.* 2011), and central Taurides, Turkey (Groves *et al.* 2005) (Figures 1 and 4).

Downloaded by [USGS Libraries] at 12:06 18 February 2015

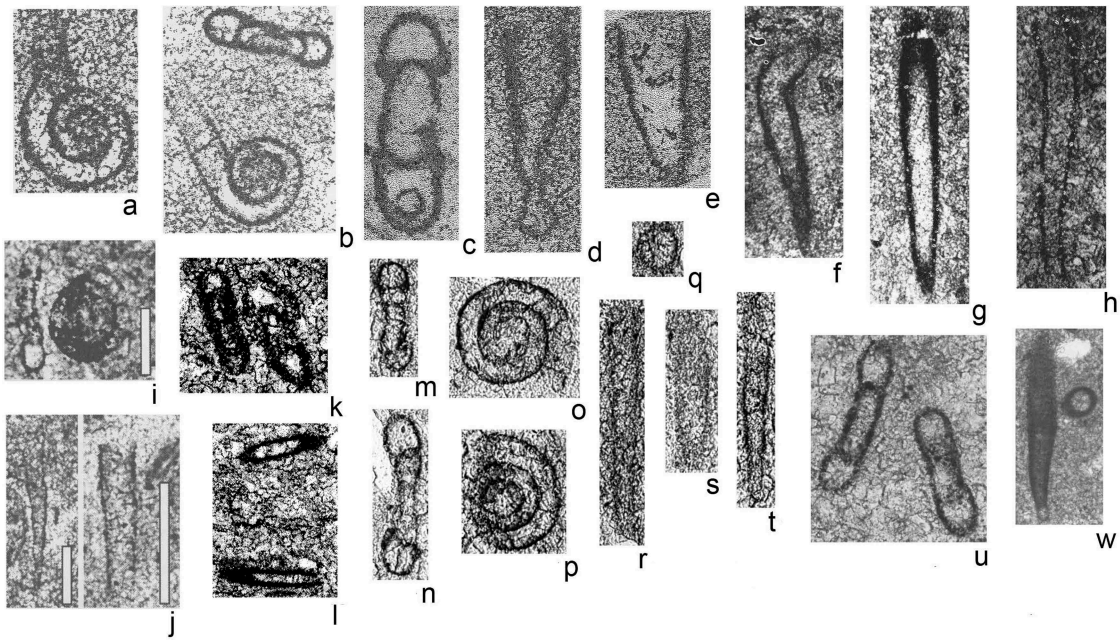


Figure 4. Representatives of *Ammodiscus kalhori* (Brönnimann, Zaninetti, and Bozorgnia) (a–c, i, k, m–p, u); *Hyperammina deformis* (Bérczi-Makk) (d–h, j, l, q–t, w), (a–e) from the Elika Formation of the central Alborz, northern Iran (after Brönnimann *et al.* 1972): (a–b) identified as *Rectocornuspira kalhori* (a is the holotype), (c) as *Cyclogyra*? *mahajeri* (holotype), (d–e) as *Earlandia tintinniformis*; (f–h) from the Bükk Mountains, northern Hungary (after Bérczi-Makk 1987): (f) identified as *Earlandia deformis* (holotype), (g) as *Earlandia dunningtoni*, (h) as *Earlandia tintinniformis*; (i–j) from the Dajiang section, Great Bank of Guizhou, Nanpanjiang Basin, South China (after Song *et al.* 2009): (i) identified as *R. kalhori*, (j) as *Earlandia* sp.; (k–l) from the Bulla and Tesero sections, southern Alps, northern Italy (after Groves *et al.* 2007): (k) identified as *R. kalhori*, (l) as *Earlandia* sp.; (m–t) from the Lukač section, western Slovenia (after Nestell *et al.* 2011): (m–p) identified as '*Cornuspira*' *mahajeri*, (q–t) as '*Earlandia*' *gracilis*; (u–w) from the Demirtaş and Taşkent sections, central Taurides, Turkey (after Groves *et al.* 2005): (u) identified as *R. kalhori*, (w) as *Earlandia* sp. Scale bar 100 μm, except (a–h, k–w) not to scale.

Twenty-eight bulk samples, covering an interval ~4 m thick through the PTB (beds 5–31; samples VN-5 through VN-31), were collected from the Lung Cam section (Figure 2). Thin sections were made from these samples, and parts of the samples were dissolved to extract the conodonts. The microfossil assemblage contains diagnostic conodonts along with ostracodes, microgastropods, microconchids and foraminifers whose free shells were found in the residues. Conodonts are present in beds 20, 22, 23, 26, and 28, with several *Hindeodus* species present in bed 20; the lowest occurrence of *H. parvus* is in the microgastropod-rich bed 28 (Figure 3, p). Microconchids occur in almost all of the residues from beds 15 to 30 and are represented by the species *Microconchus phlyctaena* (Brönnimann and Zaninetti), *M.* aff. *M. aberrans* (Hohenstein), and *M.* sp. Foraminifers are diverse and abundant in the lower part of the section (beds 6–11) and are represented by the typical latest Changhsingian fusulinaceans, *Sphaerulina* and *Nankinella*, and species of small foraminifers of genera such as *Globivalvulina*, *Dagmarita*, *Paradagmarita*, *Paraglobivalvulina*, *Paraglobivalvulinoides*, *Frondina*, *Geinitzina*, and *Pachyphloia* (Figure 2). In the upper part of the section, from bed 14 and up to bed 31, the diversity of foraminifers changes drastically. The rich late Changhsingian assemblage is replaced by tiny tests of *Ammodiscus kalhori* (Brönnimann, Zaninetti, and Bozorgnia) and *Hyperammina deformis* (Bérczi-Makk) with rare remnants of representatives of the genera *Globivalvulina*, *Nodosaria*, and *Geinitzina* in beds 14–20. The Lung Cam section presents an expanded record of the Permian–Triassic transition and contains better evidence of the succession of events than at the Meishan section in China. In the Lung Cam section, the stepwise extinction of the majority of Permian foraminiferal species occurs in beds 10 and 11 (Figure 2).

2.3. The establishment of PTB in the Lung Cam section

The correlation to a GSSP is difficult and is not always based on the local first occurrence of the boundary-identifying taxa. Therefore, correlation techniques, such as graphic correlation (Shaw 1964; Edwards 1984, 1989) or constrained optimization (Kemple *et al.* 1995; Sadler 2004), should be used in identifying the PTB in all sections other than the GSSP. Herein, a graphic correlation is applied utilizing the conodont distribution and extinction

Downloaded by [USGS Libraries] at 12:06 18 February 2015

events at Lung Cam, together with the conodont distribution at Meishan, and the extinction event there. The distribution data at Meishan are based on data from Mei *et al.* (1998), Nicoll *et al.* (2002), the Lopingian Stratigraphy and Events Workshop (Wang and Henderson 2003), and Zhang *et al.* (2007). Graphic correlation places the PTB as defined at Meishan at the base of bed 28 and the first occurrence of *H. parvus* in the Lung Cam section (Figure 2).

3. Materials and methods

3.1. Raman spectroscopy

Selected foraminiferal tests were used for surface as well as confocal Raman spectroscopic analyses using a Thermo Scientific DXR™xi Raman Imaging Microscope, fitted with OMNIC™xi Raman imaging software. Tests were oriented and fixed in desired positions on the stage, imaged, and scanned using 100 × objectives. The Raman spectra were obtained using an argon ion laser (532 nm) with a power of 9.9 mW and using an aperture spot of 50μ. The spectra (number of scans = 20) were obtained with a data acquisition time of 2.5 ms/spectra at 400 Hz using a spectral window of 200–3400 cm^{-1}. Surface as well as confocal imaging analyses were performed for element identification and mapping.

3.2. Energy-dispersive X-ray spectroscopy (EDX) analysis

Preparation involved placing the free specimen of foraminifer on an aluminium stub. Microscopic imaging was performed using an ASPEX/FEI personal scanning electron microscope. The SEM was operated in variable pressure mode and specimen images were obtained from the backscatter electron collection. Specimen composition information was determined by EDX operating in tandem with the SEM. An ASPEX OmegaMax™ silicon drift detector with an ultra-thin window (permitting light element detection) was used. The SEM standard operating conditions were an accelerating voltage of 25 keV, a beam current of approximately 1 nA, and a working distance of approximately 16 mm; X-ray acquisition was accomplished with the primary beam in spot mode.

3.3. Lead isotope analysis

Present-day Pb isotope ratios of two foraminiferal tests and five pyrite clusters samples from the Vietnamese PTB section were measured using a multi-collector thermal ionization mass spectrometer (VG sector TIMS) at the University of Rochester using NBS-981 as the Pb standard. The selected pyrite clusters were dissolved using nitric acid (HNO_3), and the foraminiferal tests in a combination of hydrofluoric acid, HNO_3, and hydrochloric acid. Pb was separated by ion-exchange chromatography using hydrobromic acid as the eluting agent. The dried samples were loaded onto Re centre filaments following the silica-gel technique (Sharma *et al.* 1992) for mass spectrometric isotopic analysis. Filament temperatures were continuously monitored during Pb isotopic measurements to correct for temperature-dependent mass fractionations. Replicate analysis of NBS-981 gave an error less than 0.10, 0.15, and 0.2% per amu (2σ) for $^{206}Pb/^{204}Pb$, $^{207}Pb/^{204}Pb$, and $^{208}Pb/^{204}Pb$, respectively.

3.4. Carbon isotope analysis

$\delta^{13}C$ values show several trends that are assumed to be real, and others that are interpreted as not reflecting global effects (Figure 5). In the Lung Cam section, the species *A. kalhori* and *H. deformis* first appear in bed 15 just above the sideritic/ankeritic limestone in bed 14 (Figure 2) where a sharp negative peak of the carbon isotope ($\delta^{13}C = -3.3‰$) is observed (Figure 5). We equate this $\delta^{13}C$ peak at Lung Cam to be equivalent to the $\delta^{13}C$ peak observed at the Meishan GSSP in bed 27a (Yin *et al.* 2001). At Lung Cam, from bed 15 to 24, the carbon isotope curve oscillates around 0‰, indicating a somewhat stable environment. From bed 25 to 32, the curve has a small negative shift reaching almost –1.1‰ in bed 28, the bed with the first appearance of abundant *H. parvus*.

3.5. Magnetic susceptibility (χ)

All materials are 'susceptible' to becoming magnetized in the presence of an external magnetic field. The initial low-field bulk, mass-specific magnetic susceptibility (χ) is an indicator of the strength of this transient magnetization. χ is very different from remanent magnetization (RM), the intrinsic magnetization that accounts for the magnetostratigraphic polarity of rocks. χ in marine stratigraphic sequences is generally considered to be an indicator of the content of detrital iron-containing paramagnetic and ferrimagnetic grains, including ferrimagnesian and clay minerals, and can be quickly and easily measured on small friable samples. In the very low inducing magnetic fields that are generally applied, χ is largely a function of the concentration and composition of the magnetizable material in a sample. χ can be measured on small, irregular lithic fragments and on a highly friable material that is usually much more difficult to sample for RM measurement. Low-field χ, as used in most reported studies, is defined as the ratio of the induced magnetization (M_i or J_i) to the strength of an applied, very low-intensity, alternating magnetic field (H_j), $J_i = \chi_{ij} H_j$ (mass-specific) or $M_i = \kappa_{ij} H_j$(volume-specific).

In these expressions, magnetic susceptibility in SI units is parameterized as κ, when indicating that the measurement is

Downloaded by [USGS Libraries] at 12:06 18 February 2015

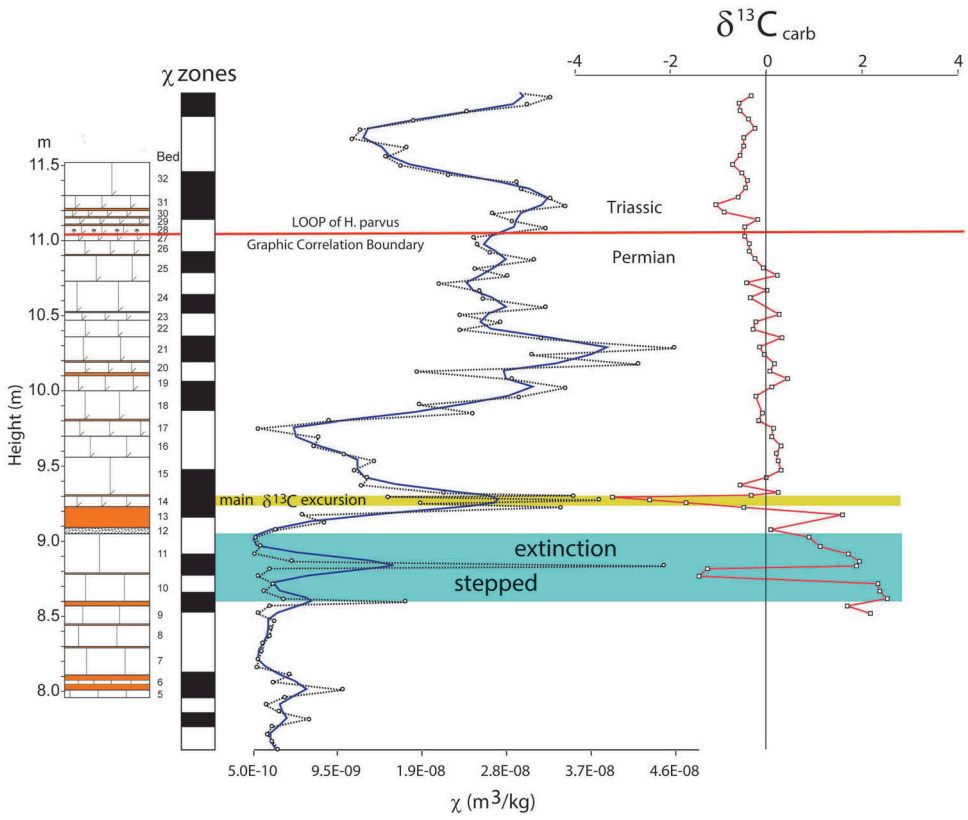


Figure 5. The Permian–Triassic succession from the Lung Cam section. Low-field, mass-specific bulk magnetic susceptibility (χ, in $m^3\ kg^{-1}$) where initial values (linked by the dotted curve) are used herein for time-series analysis; χ zone bar-logs representing spline-smoothed (solid curve) high (black) and low (white) χ values; $\delta^{13}C$ of carbonate relative to the PDB standard. $\delta^{13}C$ values are not correlated with $\delta^{18}O$, indicating that these data represent primary values. For lithological symbols, see Figure 2. LOOP, lowest observed occurrence point; H, *Hindeodus*.

relative to a 1 m^3 volume and therefore is dimensionless; magnetic susceptibility for geological materials is more generally parameterized as χ, indicating a measurement relative to a mass of 1 kg, and is given in units of $m^3\ kg^{-1}$. χ is used because it is very difficult to measure the volume of geological samples.

Values of χ for these samples are shown in the centre of Figure 6 for the ~4 m critical interval through the major extinction and PTB. These data were used to develop χ bar-log zones, indicated as horizontal black bars in the left sides of Figures 5 and 6; they act as benchmarks for dating the Lung Cam samples. The bar-log was developed from the raw χ data using smoothing splines, which were then adjusted to conform to the precessional climate cyclicity record identified in time-series results calculated from the entire ~21 m succession sampled at Lung Cam. Time-series data were developed from all samples using both Fourier transform (FT) and multitaper (MTM) methods (discussed further in Ellwood *et al.* 2013). The FT and MTM results indicate that the data are best characterized by a uniform precessional (~18 thousand years) Milankovitch climate model. This climate model is graphically drawn in Figure 6 as the alternating red and blue bands along the *X*-axis and labelled as 'P1 floating-point time-scale climate model'. We then graphically compared the χ bar-logs (zones) developed in Figure 5 (also shown in Figure 6), with the resulting intersections between the χ bar-logs and P1 model. These intersections are represented by the stippled circles in Figure 6 and result from the projection of the corresponding horizontal and vertical bar-logs for each data set. Line segments drawn through the centres of these stippled circles provide lines of correlation (LOCs) that can be used to project either data set into the other. For example, the $\delta^{13}C$ anomaly in bed 14 at Lung Cam, when projected through the LOCs and into the floating-point time scale in Figure 6, indicates that this anomaly occurred ~82 thousand years before the beginning of the Triassic. Other critical horizons are projected through the LOCs onto the horizontal axis in Figure 6, thereby determining the timing of these events at Lung Cam.

Downloaded by [USGS Libraries] at 12:06 18 February 2015

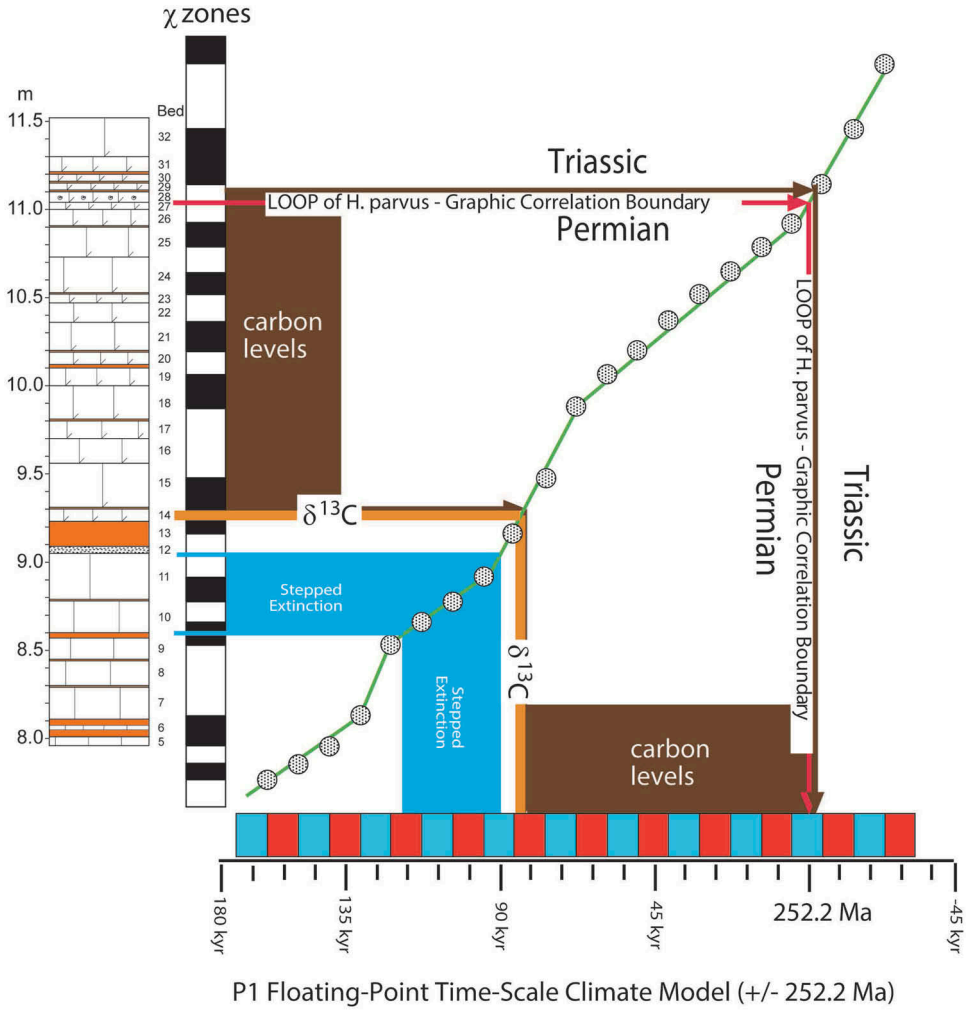


Figure 6. Floating-point time scale (FPTS) from a time-series analysis of ~400 samples collected from an ~21 m succession using raw unsmoothed magnetic susceptibility (χ) data for Lung Cam. Only ~4 m of the section is shown here. χ bar-logs (zones) constructed from the raw χ data (Figure 5) are graphically compared to a uniform Milankovitch, 18,000-year precessional climate model for the PTB interval (Berger *et al.* 1992), where each coloured bar represents ~9000 years. The intersections of the tops and bottoms of corresponding χ bar-logs and uniform climate model bar-logs are plotted as stippled dots, and a fit through these data is shown as line segments known as a lines of correlation. Using the individual segments, elements from the Lung Cam χ bar-logs are projected onto the FPTS and assigned a length of time before or after the PTB (red line). This processional climate model provides a FPTS that can be adjusted as time-scales change. In determining event ages relative to the PTB, an age of 252.2 Ma for the beginning of the Triassic was used, an age taken from the International Commission on Stratigraphy's web site hosted by Purdue University (https://engineering.purdue.edu/Stratigraphy/gssp/index.php?parentid=35). For LOOP and H., see Figure 5.

3.6. *Time-series analysis*

We have performed a time-series analysis of the primary MS data (independent of smoothing) for the sections sampled. To avoid introducing error, studied sections were selected where covered intervals could either be avoided or be sampled after careful cleaning of the section. We then collected uniformly spaced samples and assumed that this uniform spacing is linear relative to time, i.e. Δx is proportional to Δt, so that harmonic analysis methods could be used. The less this assumption is true, due to variations in sediment accumulation rate, differential diagenesis, or other factors, the more noise that will be produced in the spectral graph, and the less well defined will be spectral peaks (lower power).

The spectral power for the MS data sets was obtained using both the MTM and FT methods after the data were detrended and subjected to a Hanning window (Jenkins and Watts 1968; Thomson 1982). Incidences of statistically significant peaks (at the 90, 95, and 99% confidence limits) in the resulting spectra are determined by employing MTM (Ghil *et al.* 2002), as calculated with the SSA-MTM toolkit (Dettinger *et al.* 1995). A null hypothesis of red noise was assumed (low frequency high power in the spectrum, sloping towards lower values at high

Downloaded by [USGS Libraries] at 12:06 18 February 2015

Downloaded by [USGS Libraries] at 12:06 18 February 2015

frequencies), with a three-taper model. As this method is prone to producing false positives, we limit the use of statistical significance here to its role in supporting (or not) the positions of multiple Milankovitch bands within the data set. The positions of these bands are fixed relative to each other, and so a climate-forcing mechanism is supported by the spectral analysis when the Milankovitch frequencies are also frequencies of high spectral power. The MTM and FT methods, like the spline-smoothed MS data and bar-logs derived from these data sets, are capable of resolving high-frequency features in the data. Our approach then is to (1) collect closely and uniformly spaced samples in the field, (2) report both FT and MTM after normal detrending and comparing the two, (3) apply confidence limits to the MTM data, (4) place the important Milankovitch climate bands on the FT and MTM diagrams for consistency checks, and (5) establish a uniform model using bar logs that can then be compared to the MS cyclicity as a check on sediment accumulation rate uniformity or lack thereof. These five tests then allow rigorous evaluation of the time-series data sets developed here.

Results from the time-series analysis performed on the raw Lung Cam χ data set are summarized in Figure 7. The

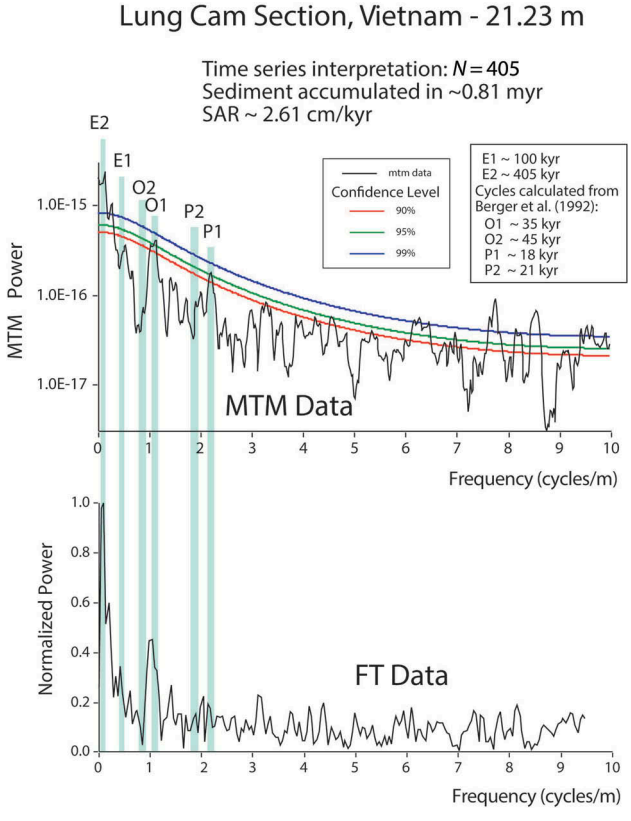


Figure 7. Time-series analysis (MTM, multitaper method; FT, Fourier transform) of the raw Lung Cam χ data set, exhibiting strong E2 Milankovitch eccentricity cyclicity, strong O1 obliquity, and P1 cyclicity. Milankovitch cycles tested for are given in the upper right in the diagram. SAR, sediment accumulation rate.

results show a strong E2 (405 thousand years; >99% confidence level) Milankovitch eccentricity cyclicity, strong O1 obliquity (~35 thousand years; >95% confidence level, and P1 (~18 thousand years; >95% confidence level) cyclicity. Values for obliquity and precession are derived from Berger *et al.* (1992). These data provide an estimate of the total time represented by the 21.23 m section at Lung Cam, of ~0.81 million years, representing a sediment accumulation rate of ~2.61 cm/thousand years. The timing and duration of these events, using our FT and MTM results, is very similar to the timing of events recently reported for the PTB interval (Song *et al.* 2009; Shen *et al.* 2011a).

3.7. *Foraminiferal study: taxonomic issues*

In many sections in the world where conodonts and ammonoids have not been found, and before the establishment of the GSSP for the lower boundary of the Triassic, the PTB was often drawn based on the first appearance of the small foraminifer species identified as '*Rectocornuspira*' *kalhori*, '*Cornuspira*' *mahajeri*, and '*Earlandia*', and also species of the microconchids *Microconchus* (given as *Spirorbis* in the literature) *phlyctaena* (Nestell *et al.* 2011). These species of foraminifers have been assigned to these genera based on the presence of a dark wall that appears to resemble the microgranular wall of calcareous Palaeozoic forms (Figures 3 and 4). Recently, the species '*Rectocornuspira*' *kalhori* and '*Cornuspira*' *mahajeri* were assigned to the genus *Postcladella* with the type species *Rectocornuspira kalhori* and '*Cornuspira*' *mahajeri* as synonyms (Krainer and Vachard 2011). A discussion of the validity of this genus is presented in Nestell *et al.* (2011).

As noted above, free specimens of the foraminifers previously identified as *Cornuspira* and *Earlandia* are present in the PTB interval at the Lung Cam section, together with conodonts, ostracodes, and microconchids of the genus *Microconchus*. Some of shells of these microfauna are black and white in colour. The wall composition of the black and white '*Earlandia*' and '*Cornuspira*' was analysed using an EDX and a DXR™xi Raman imaging microscope. The tests of the foraminifers were found to contain carbon, oxygen, and silica, but not calcium carbonate. Furthermore, the dark tests contain more carbon than the white ones (Figures 3, 8 and 9). The abundance of dark tests increases from bed 15 to bed 17, reaches a maximum in beds 17 and 18, remains high in beds 19–23, and decreases from bed 24 to bed 28. Such tests are absent in beds 29–31 where only very rare and tiny specimens of '*Cornuspira*' *mahajeri* are visible in thin sections. Both of these Lung Cam foraminiferal taxa studied by us were previously considered to belong to carbonate-walled genera, but in fact have an agglutinated wall structure. Thus, they are reassigned from *R.* (or *C.*) *kalhori* to *A. kalhori* (Brönnimann, Zaninetti, and

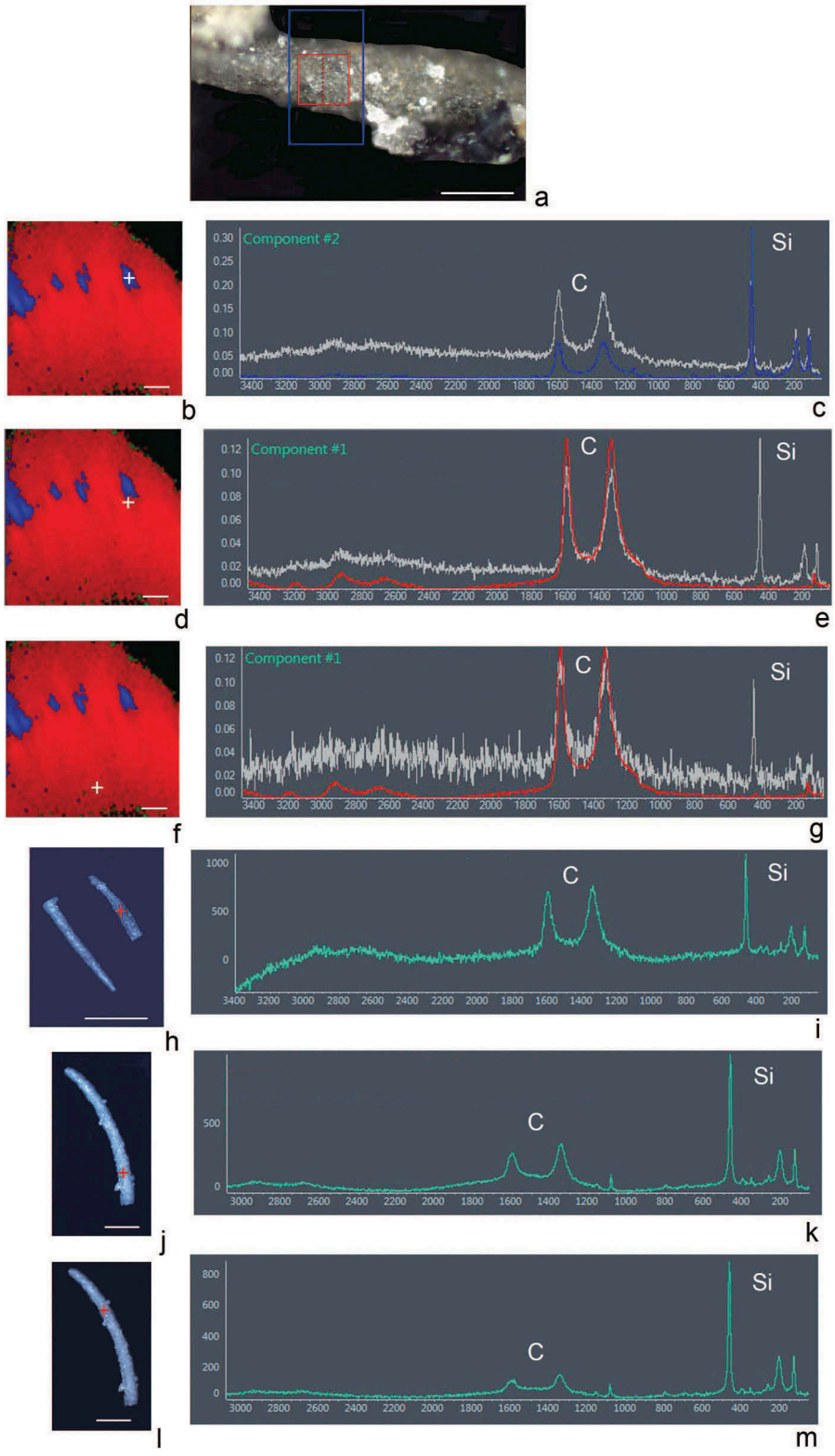


Figure 8. Images of *Hyperammina deformis* (Bérczi-Makk) from the Lung Cam section taken with a DXR™xi Raman imaging microscope. (a) Image of the part of the surface of a free dark colour test (sample VN-17) with boxes where the cross section of the test was analysed; (b, d, f) cross section of the test, red colour indicates carbon whereas dark blue colour indicates quartz grains; (c, e, g) composition of the area of the test marked by cross on (b, d, f); (h) free dark colour test from sample VN-20; (i) composition of the area of the test marked by a cross on (h); (j, l) free white colour test from sample VN-30; (k, m) composition of the area of the test marked by a cross on (j, l). Scale bars: (a) 100 μm; (b, d, f) 10 μm; (h) 500 μm; (j, l) 200 μm.

Downloaded by [USGS Libraries] at 12:06 18 February 2015

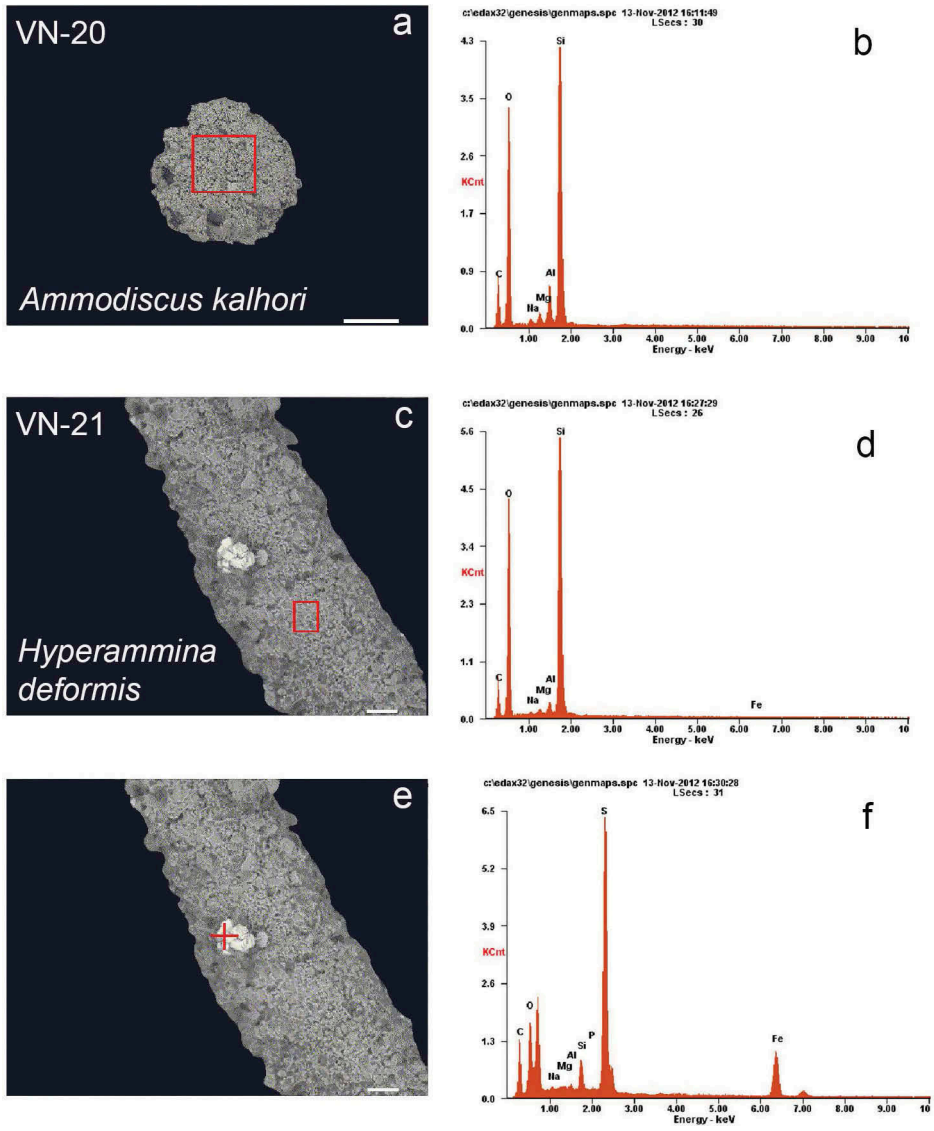


Figure 9. Backscattered electron images of *Ammodiscus kalhori* (Brönnimann, Zaninetti, and Bozorgnia) (a) and *Hyperammina deformis* (Bérczi-Makk) (c, e) with their corresponding energy-dispersive spectra indicating their chemical composition (C, Si and O) in (a, b) and (c, d), and the composition of pyrite grain (Fe, S with minor C) in (e) and (f). Scale bar: (a) 50 µm; (c, e) 10 µm.

Downloaded by [USGS Libraries] at 12:06 18 February 2015

Bozorgnia), and from *Earlandia* spp. to *H. deformis* (Bérczi-Makk). Conical tube-like taxa earlier assigned to *Aeolisaccus* or *Earlandia* from the uppermost Permian and Middle–Upper Triassic should be re-examined and the taxonomy revised because the illustrated axial sections do not show the initial chamber.

4. Discussion

Judging by the abundance of carbon particles in the walls of the agglutinated foraminifers *A. kalhori* and *H. deformis*, there clearly was a large influx of carbon into the global marine environment through the PTB time interval. The pyrite clusters attached to the wall of *H. deformis* were also analysed for Pb isotopes (Figure 10). Two black tests (one from sample VN-18 and another from sample VN-19), as well as five pyrite grains separated from these black foraminiferal tests (samples VN-18, VN-20, VN-21, VN-23, and VN-25), were subjected to high-precision Pb isotopic analysis using a thermal ionization mass spectrometer (Figure 11). Present-day $^{206}Pb/^{204}Pb$, $^{207}Pb/^{204}Pb$, and $^{208}Pb/^{204}Pb$ ratios from these analyses are shown in Table 1 and plotted in Figure 10 in conventional Pb isotope ratio plots. These data are compared with the common global crust-mantle reservoirs as shown in

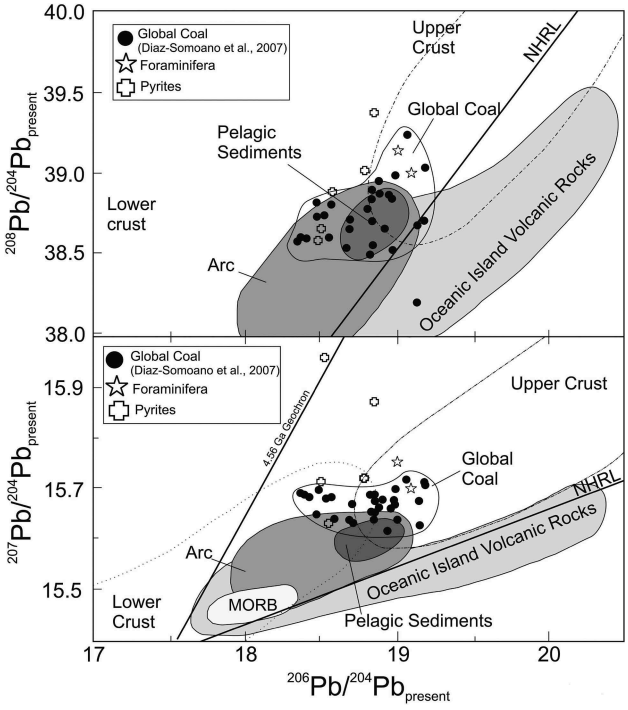


Figure 10. Results of Pb isotopic analysis of two foraminiferal tests and five associated pyrite clusters are plotted in the conventional Pb isotope ratio plots. The analysis is compared with some global reservoirs, characterized by their ranges of Pb isotopic compositions, such as lower and upper continental crust, island arc, mid-oceanic ridge basalts (MORB), pelagic sediments, ocean island volcanic rocks, global coal, and the Northern Hemisphere Reference Line (NHRL). These reservoirs are taken from the literature and are representative of Earth's crust–mantle reservoirs in Pb isotopic compositions. The 4.56 billion year geochron along which primitive Earth lies is also shown.

Figure 10, which also includes the 4.56 Ga geochron as a reference for primitive bulk Earth in Pb isotope ratios. A new reservoir, Global Coal, was added in this diagram of Pb isotopic compositions of coal from different continents (Díaz-Somoano *et al.* 2007). Note the closely distributed field of global coal from Australia, Hungary, Canada, Indonesia, North America, Peru, Romania, South Africa, and Spain in Figure 10, which also includes the two foraminiferal tests (noted as stars) and most of the associated pyrite grains (noted as crosses) reported herein. Most importantly, the foraminiferal tests and their pyrite clusters are compared with the isotopic ranges of global coal deposits from different continents. The similarity between the coal and the foraminiferal tests is remarkable. The only exceptions are the two pyrite analyses with anomalously high $^{207}Pb/^{204}Pb$ ratios. The restricted range in Pb isotope ratios of global coal of different continents is interpreted to be due to the common Carboniferous–Permian age of most coal deposits in sedimentary fluvial environments of continents with an average age of 2 billion years.

The Pb isotopic data of Figure 10 can best be interpreted based on the assumption that the black foraminiferal tests inherited the Pb in their outer layer and also perhaps in the inner carbon-poor, silica-rich tests from carbon-contaminated seawater (Figures 3 and 9). The source of the carbon could be either global coal fly ash in the oceans or global forest fire-dispersed carbon, or both, in the world's oceans after the end-Permian extinction event. This conclusion is based on observations of blackened foraminiferal tests restricted to beds 15–28, all above the stepped extinction interval in the Lung Cam section, and observations from the literature of similar blackened foraminiferal tests from the late Permian Palaeo-Tethys Ocean (Figures 1 and 4). Although only two foraminiferal tests were analysed (VN-18 and VN-19), five associated pyrite clusters were also analysed, one of which was obtained from VN-18 tests. These pyrite clusters (Figures 9 and 11) presumably formed by early diagenesis during euxinic conditions on the seabed with a carbon-enriched seawater column. Hudspith *et al.* (2014) recently proposed that the chars in latest Permian marine sediments may have been derived from wildfires and not from the combustion of coal. However, our data from the pyrite clusters support the presence of products of coal combustion in the Lung Cam section.

The foraminiferal species *A. kalhori* and *H. deformis* are considered to be opportunistic organisms that usually appear during a biotic crisis connected with a stressful environment and are characterized by very simple morphology and small size (MacArthur 1955; Hallam and Wignall 1997). The appearance of the microconchids *M. phlyctaena* that usually colonized freshwater, brackish, and hypersaline environments (Vinn 2010), together with the foraminifers, also indicate a stressful environment following the major stepped extinction in beds 10 and 11 in the Lung Cam section (Figure 2). The foraminiferal genera *Geinitzina* and *Globivalvulina* are considered to be holdover taxa that persisted into bed 15 (*Geinitzina*) and bed 20 (*Globivalvulina*) and became extinct in the survival phase of the extinction, whereas representatives of the genus *Nodosaria*, *A. kalhori*, and *H. deformis* can be assigned to progenitor taxa, which radiated in the recovery phase after the Permian–Triassic extinction (Hallam and Wignall 1997). It should be noted that the species *A. kalhori*, *H. deformis*, and *M. phlyctaena* appeared long before the first occurrence of *H. parvus* in the Lung Cam section. Their appearance coincided with the onset of a stressful environment, indicating the environmental control on these species. Thus, the finding of these species in PTB sections cannot be the basis for defining the PTB worldwide (Nestell *et al.* 2011).

The transition to a foraminiferal fauna dominated by small-sized *Ammodiscus* (an active deposit-feeder) and *Hyperammina* (a suspension-feeder) (Jones and Charnock 1985; Jorissen *et al.* 1995) with a significant amount of

Downloaded by [USGS Libraries] at 12:06 18 February 2015

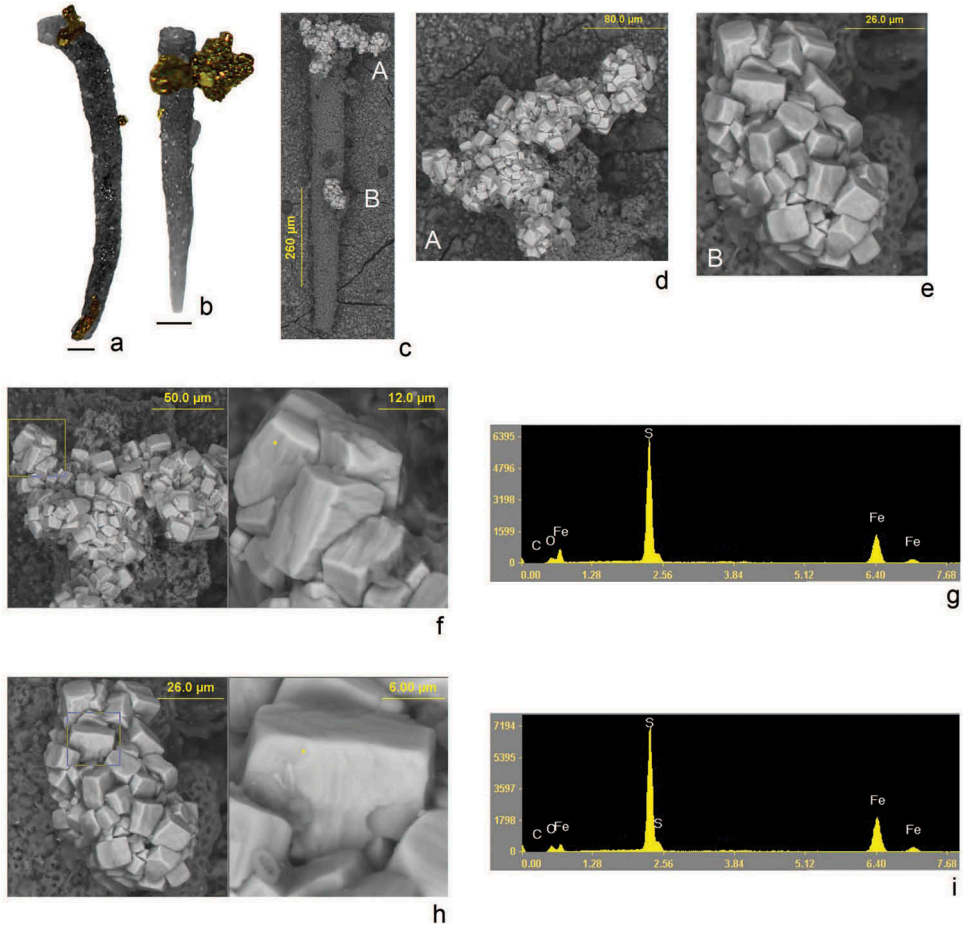


Figure 11. Tests of species *Hyperammina deformis* (Bérczi-Makk) (a–c) covered with carbon (dark in appearance) and attached pyrite clusters (a, b), and SEM photomicrograph with two (A, B) attached pyrite clusters (c). (d) SEM photomicrograph of the A cluster, (f) backscattered electron image of the A cluster and (g) energy-dispersive X-ray spectrum from points in the selected area (scan box) of the A cluster; (e) SEM photomicrograph of the B cluster, (h) backscattered electron image of the B cluster; and (i) energy-dispersive X-ray spectrum from points in the selected area (scan box) of the B cluster. (a, c) Sample VN-23; (b) sample VN-20. Scale bar 100 µm for (a, b).

Table 1. Measured Pb isotopic data for foraminifers and pyrite clusters from the PTB interval in the Lung Cam section.

Fossil ID	$^{206}Pb/^{204}Pb_{(m)}$	$^{207}Pb/^{204}Pb_{(m)}$	$^{208}Pb/^{204}Pb_{(m)}$
VN-18 foram	19.006	15.755	39.135
VN-19 foram	19.096	15.703	38.995
VN-18 pyrite	18.503	15.715	38.587
VN-20 pyrite	18.525	15.960	38.659
VN-21 pyrite	18.851	15.873	39.368
VN-23 pyrite	18.787	15.722	39.008
LC-25 pyrite	18.575	15.635	38.876

carbon in the wall structure indicates that there must have been a large flux of carbon introduced into the marine environment. This flux is also evidenced by a negative shift of $\delta^{13}C$ in bed 14 as seen in the curve constructed for the Lung Cam section (Figure 5). The small size and increased abundance of only two opportunistic species of foraminifers could be a result of rapid reproduction as an adaptation to a drastic change in environmental conditions and the loss of calcareous foraminifers as competitors. A similar widespread response to an environmental change in seafloor conditions occurred in the populations of the agglutinated foraminiferal genera *Glomospira* and

Downloaded by [USGS Libraries] at 12:06 18 February 2015

Downloaded by [USGS Libraries] at 12:06 18 February 2015

Repmanina at the Palaeocene–Eocene boundary. This change is found in association with a worldwide thermal maximum event, and resulting '*Glomospira* acme' zone including species of three genera *Glomospira*, *Glomospirella*, and *Repmanina* (all epifaunal active or passive deposit feeders). Both the Permian–Triassic and Palaeocene–Eocene extinction events are related to stressed environments resulting from rapidly changing seafloor conditions. Because of their feeding preferences, benthic foraminiferal populations were able to take advantage of the increase in organic matter on the seafloor, allowing them to populate empty post-extinction niches (Arreguin-Rodriguez *et al.* 2013).

In order to evaluate the timing of events relative to the PTB at Lung Cam, time-series analyses were applied to the magnetic susceptibility data from ~400 samples collected at 0.05 m intervals throughout the ~21 m succession at Lung Cam. The stepped extinction began in bed 10, the base of which, according to time-series analysis, took place ~119 thousand years before the PTB, with the extinction event lasting through bed 11, a time-span of ~28 thousand years, ending at the top of bed 11, ~91 thousand years before the PTB. The negative $\delta^{13}C$ anomaly discussed above, which occurred in bed 14, beginning at ~85.5 thousand years before the boundary, had its negative peak ~8 thousand years after the last major extinction in bed 11. The PTB, identified by graphic correlation (Figures 5 and 6), lies in bed 28 at Lung Cam, coincident with the first occurrence of *H. parvus*. The charcoal levels at Lung Cam began at the base of bed 15 at ~82 thousand years below the PTB, but became well defined in bed 17 at ~72 thousand years below the boundary. Charcoal content is continuous in the section to the top of bed 28, at ~ 3 thousand years above the PTB. It is important to note that the timing and duration of these events, as revealed by our FT and MTM results, are very similar to the timing and duration of events through the PTB interval (Song *et al.* 2013; using absolute ages from Shen *et al.* 2011a).

5. Conclusion

J. Shen *et al.* (2012) noted a sharp increase in charcoal in a basinal marine section in South China at the end-Permian extinction event, which they attributed to increased wildfire intensity. We contend that charcoal influx into the ocean environment was so intense that there was an excess amount of carbon in the ocean floor sediments which permitted its incorporation into the wall of the agglutinated foraminifers. For the first time, we were able to extract free tests of foraminifers from strata of the Permian–Triassic transition interval in the Lung Cam section, northern Vietnam. All foraminifers previously illustrated from PTB sections worldwide have been studied in thin sections where oriented sections of the tests were difficult to obtain. Thus, proper assignments of taxa to the species and genus level were difficult. By having free tests of foraminifers, and using EDX and laser Raman microscopy on these tests, we found that they contain only carbon, oxygen, and silica, and do not contain any calcium carbonate. From this evidence, we concluded that these foraminifers are clearly of 'agglutinated' type and should not be considered as 'carbonate' genera, as has been previously suggested in numerous publications. Such 'carbonate' foraminifers with blackened tests, as shown in thin sections, are widespread in the PTB strata globally, and known in many sections of Slovenia, Italy, Austria, Hungary, Turkey, Iran, and South China. These foraminifers, identified previously as *R. kalhori* Brönnimann, Zaninetti, and Bozorgnia, *C. mahajeri* Brönnimann, Zaninetti, and Bozorgnia, and *Earlandia* spp. from many PTB interval sections of different regions of the Palaeo-Tethys Ocean, now are referred to as *A. kalhori* (Brönnimann, Zaninetti, and Bozorgnia) with *C. mahajeri* Brönnimann, Zaninetti, and Bozorgnia as its synonym, and *H. deformis* (Bérczi-Makk).

Besides analysing the presence of carbon in the wall structure of the foraminifers, pyrite clusters attached to the wall of *H. deformis* were also analysed for Pb isotopes. Present-day $^{206}Pb/^{204}Pb$, $^{207}Pb/^{204}Pb$, and $^{208}Pb/^{204}Pb$ ratios from these analyses are compared with the isotopic ranges of global coal deposits from different continents, and the similarity of the Pb isotope ratios between the coal and the pyrite clusters attached to the foraminiferal tests is remarkable. These pyrite clusters presumably formed by early diagenesis during euxinic conditions on the seabed with a carbon-enriched seawater column. Data from the pyrite clusters support the presence of products of coal combustion in the Lung Cam section, not wildfires. However, the source of the carbon could have been global coal fly ash or forest fire-dispersed carbon, or a combination of both, which accumulated in the Palaeo-Tethys Ocean immediately after the end-Permian extinction.

According to time-series analysis, the stepped extinction at the Lung Cam section began (bed 10) ~119 thousand years before the PTB. The extinction event lasted ~28 thousand years and ended at ~91 thousand years before the PTB (top bed 11). The charcoal levels at Lung Cam began at the base of bed 15 at ~82 thousand years below the PTB and continued to the top of bed 28 at ~3 thousand years above the PTB.

Acknowledgements

We thank Sue Ellwood for designing the sample method used and her aid in sampling. LTPL thanks Dr Dang Tran Huyen for his help in understanding the palaeobiology in the Lung Cam section. Drs B. Sen Gupta (Louisiana State University), M. Robinson (US Geological Survey), and V. Vuks (VSEGEI, Saint Petersburg, Russia) are graciously thanked for their constructive and valuable comments, which improved the manuscript. We are grateful to Dr R. Blakey (Northern Arizona University) for providing literature and a palaeogeographical

map for the late Permian. We thank the Editor-in-Chief, Dr R. Stern, for suggestions to improve the manuscript.

Disclosure statement

Any use of trade, firm, or product is for descriptive purposes only and does not imply endorsement by US Government.

Funding

This work was partly supported by the National Science Foundation [grant number EAR-0745393]. LTPL thanks the Vietnam Institute of Geophysics for partial funding for this project.

References

Algeo, T., Shen, Y., Zhang, T., Lyons, T., Bates, S., Rowe, H., and Nguyen, T.K.T., 2008, Association of ^{34}S-depleted pyrite layers with negative carbonate δ^{13}C excursions at the permian-triassic boundary: Evidence for upwelling of sulfidic deep-ocean water masses: Geochemistry, Geophysics, Geosystems, v. 9, p. 1–10. doi:10.1029/2007GC001823

Algeo, T.J., Ellwood, B.B., Nguyen, T.K.T., Rowe, H., and Maynard, J.B., 2007, The Permian–Triassic boundary at Nhi Tao, Vietnam: Evidence for recurrent influx of sulfidic watermasses to a shallow-marine carbonate platform: Palaeogeography, Palaeoclimatology, Palaeoecology, v. 252, p. 304–327. doi:10.1016/j.palaeo.2006.11.055

Arreguin-Rodriguez, G.J., Alegret, L., and Ortiz, S., 2013, *Glomospira* acme during the Paleocene-Eocene thermal maximum: Response to $Caco_3$ dissolution or to ecological forces? Journal of Foraminiferal Research, v. 43, p. 40–54.

Basu, A.R., Petaev, M.I., Poreda, R.J., Jacobsen, S.B., and Becker, L., 2003, Chondritic meteorite fragments associated with the Permian-Triassic boundary in Antarctica: Science, v. 302, p. 1388–1392. doi:10.1126/science.1090852

Becker, L., Poreda, R.J., Hunt, A.G., Bunch, T.E., and Rampino, M., 2001, Impact event at the Permian-Triassic boundary: Evidence from extraterrestrial noble gases in fullerenes: Science, v. 291, p.1530–1533. doi:10.1126/science.1057243

Bérczi-Makk, A., 1987, *Earlandia* (Foraminifera) species from the Permian-Triassic boundary in N Hungary: Magyar Állami Földtani Intézet evi Jelentése Az 1985, Évről, v. 1987, p. 215–226.

Berger, A., Loutre, M.F., and Laskar, J., 1992, Stability of the astronomical frequencies over the Earth's history for paleoclimate studies: Science, v. 255, p. 560–566. doi:10.1126/science.255.5044.560

Berner, R.A., 2002, Examination of hypotheses for the Permo-Triassic boundary extinction by carbon cycle modeling: Proceedings of the National Academy of Sciences, v. 99, p. 4172–4177. doi:10.1073/pnas.032095199

Blakey, R.C., 2003, Carboniferous-Permian paleogeography of the assembly of Pangaea, *in* Proceedings of the XVth International Congress on Carboniferous and Permian Stratigraphy, Utrecht, The Netherlands, 10–16 August, Royal Netherlands Academy of Arts and Sciences: Chicago, Illinois, University of Chicago Press, p. 443–456.

Brand, U., Posenato, R., Came, R., Affek, H., Angiolini, L., Azmy, K., and Farabegoli, E., 2012, The end-Permian mass extinction: A rapid volcanic CO_2 and CH_4-climatic catastrophe: Chemical Geology, v. 322–323, p. 121–144. doi:10.1016/j.chemgeo.2012.06.015

Brönnimann, P., Zaninetti, L., and Bozorgnia, F., 1972, Triassic (Scythian) smaller foraminifera from the Elika formation of the central Alborz, northern Iran, and from the Siusi formation of the Dolomites, northern Italy: Mitteilungen Der Gessellschaft Der Geologie Und Bergbaustudenten, v. 21, p. 861–884.

Dettinger, M.D., Ghil, M., Strong, C.M., Weibel, W., and Yiou, P., 1995, Software expedites singular-spectrum analysis of noisy time series: Eos Transactions of the American Geophysical Union, v. 76, p. 12–21.

Díaz-Somoano, M., Kylander, M., Weiss, D.J., López-Antón, M. A., Suárez-Ruiz, I., and Martínez-Tarazona, M.R., 2007, Lead isotope variability in different world wide coal deposits, *in* International Conference on Coal Science and Technology, Nottingham, 28–31 August, CD-paper 2P2.

Edwards, L.E., 1984, Insights on why graphic correlation (Shaw's method) works: The Journal of Geology, v. 92, p. 583–597. doi:10.1086/628893

Edwards, L.E., 1989, Supplemented graphic correlation: A powerful tool for paleontologists and nonpaleontologists: Palaios, v. 4, p. 127–143. doi:10.2307/3514601

Ellwood, B.B., Brett, C.E., Tomkin, J.H., and MacDonald, W.D., 2013, Visual identification and quantification of Milankovitch climate cycles in outcrop: An example from the Upper Ordovician Kope Formation, Northern Kentucky, *in* Jovane, L., Herrero–Bervera, E., Hinnov, L.A., and Housen, B.A., eds., Magnetic methods and timing of geological processes: The Geological Society of London Special Publications, Volume 373, p. 341–353. doi:doi.org/10.1144/SP373.2

Ghil, M., Allen, R.M., Dettinger, M.D., Ide, K., Kondrashov, D., Mann, M.E., Robertson, A., Saunders, A., Tian, Y., Varadi, F., and Yiou, P., 2002, Advanced spectral methods for climatic time series: Reviews of Geophysics, v. 40, p. 3.1–3.41. doi:10.1029/2000RG000092

Grasby, S.E., Sanei, H., and Beauchamp, B., 2011, Catastrophic dispersion of coal fly ash into oceans during the latest Permian extinction: Nature Geoscience, v. 4, p. 104–107. doi:10.1038/ngeo1069

Groves, J.R., Altiner, D., and Rettori, R., 2005, Extinction, survival, and recovery of lagenide foraminifers in the Permian-Triassic boundary interval, Central Taurides, Turkey: Journal of Paleontology, v. 79, no. sp62, p. 1–38. doi:10.1666/0022-3360(2005)79[1:ESAROL]2.0.CO;2

Groves, J.R., Rettori, R., Payne, J.L., Boyce, M.D., and Altiner, D., 2007, End-Permian mass extinction of lagenide foraminifers in the Southern Alps (northern Italy): Journal of Paleontology, v. 81, p. 415–434. doi:10.1666/05123.1

Hallam, A., and Wignall, P.B., 1997, Mass extinctions and their aftermath: Oxford, Oxford University Press, p. 320.

Hallam, A., and Wignall, P.B., 1999, Mass extinctions and sea-level changes: Earth Science Reviews, v. 48, p. 217–250. doi:10.1016/S0012-8252(99)00055-0

Hudspith, V.A., Rimmer, S.M., and Belcher, C.M., 2014, Latest Permian chars may derive from wildfires, not coal combustion: Geology, v. 42, p. 879–882. doi:10.1130/G35920.1

Isozaki, Y., 1997, Permo-Triassic boundary superanoxia and stratified superocean: Records from lost deep sea: Science, v. 276, p. 235–238. doi:10.1126/science.276.5310.235

Jenkins, G.M., and Watts, D.G., 1968, Spectral analysis and its applications: San Francisco, Holden-Day, p. 525.

Joachimski, M.M., Lai, X., Shen, S., Jiang, H., Luo, G., Chen, B., Chen, J., and Sun, Y., 2012, Climate warming in the

Downloaded by [USGS Libraries] at 12:06 18 February 2015

latest Permian and the Permian-Triassic mass extinction: Geology, v. 40, p. 195–198. doi:10.1130/G32707.1

Jones, R.W., and Charnock, M.A., 1985, 'Morphogroups' of agglutinating Foraminifera: Their life positions and feeding habits and potential applicability in (paleo)ecological studies: Revue De Paléobiologie, v. 42, p. 311–320.

Jorissen, F.J., De Stigter, H.C., and Widmark, J.G.V., 1995, A conceptual model explaining benthic foraminiferal microhabitats: Marine Micropaleontology, v. 26, p. 3–15. doi:10.1016/0377-8398(95)00047-X

Kaiho, K., Kajiwara, Y., Nakano, T., Miura, Y., Kawahata, H., Tazaki, K., Ueshima, M., Chen, Z., and Shi, G.R., 2001, End-Permian catastrophe by a bolide impact: Evidence of a gigantic release of sulfur from the mantle: Geology, v. 29, p. 815–818. doi:10.1130/0091-7613(2001)029<0815:EPCBAB>2.0.CO;2

Kaiho, K., Oba, M., Fukuda, Y., Ito, K., Ariyoshi, S., Gorjan, P., Riu, Y., Takahashi, S., Chen, Z.-Q., Tong, J., and Yamakita, S., 2012, Changes in depth-transect redox conditions spanning the end-Permian mass extinction and their impact on the marine extinction: Evidence from biomarkers and sulfur isotopes: Global and Planetary Change, v. 94–95, p. 20–32. doi:10.1016/j.gloplacha.2012.05.024

Kamo, S.L., Czamanske, G.K., Amelin, Y., Fedorenko, V.A., Davis, D.W., and Trofimov, V.R., 2003, Rapid eruption of Siberian flood-volcanic rocks and evidence for coincidence with the Permian-Triassic boundary and mass extinction at 251 Ma: Earth and Planetary Science Letters, v. 214, p. 75–91. doi:10.1016/S0012-821X(03)00347-9

Kemple, W.G., Sadler, P.M., and Strauss, D.J., 1995, Extending graphic correlation to many dimensions: Stratigraphic correlation as constrained optimization, *in* Mann, K.O., and Lane, H.R., eds., Graphic correlation: Society of Economic Paleontologists and Mineralogists Special Publication, Volume 53, p. 65–82.

Kidder, D.L., and Worsley, T.R., 2004, Causes and consequences of extreme Permo-Triassic warming to globally equable climate and relation to the Permo-Triassic extinction and recovery: Palaeogeography, Palaeoclimatology, Palaeoecology, v. 203, p. 207–237. doi:10.1016/S0031-0182(03)00667-9

Knies, J., Grasby, S.E., Beauchamp, B., and Schubert, C.J., 2013, Water mass denitrification during the latest Permian extinction in the Sverdrup Basin, Arctic Canada: Geology, v. 41, p. 167–170. doi:10.1130/G33816.1

Korte, Ch., Pande, P., Kalia, P., Kozur, H.W., Joachimski, M.M., and Oberhänsli, H., 2010, Massive volcanism at the Permian-Triassic boundary and its impact on the isotopic composition of the ocean and atmosphere: Journal of Asian Earth Sciences, v. 37, p. 293–311. doi:10.1016/j.jseaes.2009.08.012

Krainer, K., and Vachard, D., 2011, The Lower Triassic Werfen Formation of the Karawanken Mountains (Southern Austria) and its disaster survivor microfossils, with emphasis on *Postcladella* n. gen. (Foraminifera, Miliolata, Cornuspirida): Revue De Micropaléontologie, v. 54, p. 59–85. doi:10.1016/j.revmic.2008.11.001

MacArthur, R.H., 1955, Fluctuations of animal populations and a measure of community stability: Ecology, v. 36, p. 533–536. doi:10.2307/1929601

Mei, S., Zhang, K., and Wardlaw, B.R., 1998, A refined succession of Changhsingian and Griesbachian neogondolellid conodonts from the Meishan section, candidate of the global stratotype section and point of the Permian-Triassic boundary: Palaeogeography, Palaeoclimatology, Palaeoecology, v. 143, p. 213–226. doi:10.1016/S0031-0182(98)00112-6

Nestell, G.P., Kolar-Jurkovšek, T., Jurkovšek, B., and Aljinović, D., 2011, Foraminifera from the Permian-Triassic transition in western Serbia: Micropaleontology, v. 57, p. 197–222.

Newton, R.J., Pevitt, E.L., Wignall, P.B., and Bottrell, S.H., 2004, Large shifts in the isotopic composition of seawater sulphate across the Permo-Triassic boundary in northern Italy: Earth and Planetary Science Letters, v. 218, p. 331– 345. doi:10.1016/S0012-821X(03)00676-9

Nicoll, R.S., Metcalfe, I., and Wang, C.Y., 2002, New species of the conodont genus *Hindeodus* and the conodont biostratigraphy of the Permian-Triassic boundary interval: Journal of Asian Earth Sciences, v. 20, p. 609–631. doi:10.1016/S1367-9120(02)00021-4

Ogden, D.E., and Sleep, N.H., 2012, Explosive eruption of coal and basalt and the end-Permian mass extinction: Proceedings of the National Academy of Sciences, v. 109, p. 59–62. doi:10.1073/pnas.1118675109

Raup, D.M., 1979, Size of the Permo-Triassic bottleneck and its evolutionary implications: Science, v. 206, p. 217–218. doi:10.1126/science.206.4415.217

Renne, P.R., and Basu, A.R., 1991, Rapid eruption of the Siberian traps flood basalts at the Permo-Triassic boundary: Science, v. 253, p. 176–179. doi:10.1126/science.253.5016.176

Renne, P.R., Black, M.T., Zichao, Z., Richards, M.A., and Basu, A.R., 1995, Synchrony and causal relations between Permian-Triassic boundary crises and Siberian flood volcanism: Science, v. 269, p. 1413–1416. doi:10.1126/science.269.5229.1413

Riccardi, A.L., Arthur, M.A., and Kump, L.R., 2006, Sulfur isotopic evidence for chemocline upward excursions during the end-Permian mass extinction: Geochimica Et Cosmochimica Acta, v. 70, p. 5740–5752. doi:10.1016/j.gca.2006.08.005

Sadler, P.M., 2004, Quantitative biostratigraphy—Achieving finer resolution in global correlation: Annual Review of Earth and Planetary Sciences, v. 32, p. 187–213. doi:10.1146/annurev.earth.32.101802.120428

Sharma, M., Basu, A.R., and Nesterenko, G., 1992, Temporal Sr-, Nd- and Pb-isotopic variations in the Siberian flood basalts: Implications for the plume-source characteristics: Earth and Planetary Science Letters, v. 113, p. 365–381. doi:10.1016/0012-821X(92)90139-M

Shaw, A.B., 1964, Time in stratigraphy: New York, McGraw-Hill, p. 365.

Shen, J., Algeo, T.J., Hu, Q., Xu, G., Zhou, L., and Feng, Q., 2013, Volcanism in South China during the late Permian and its relationship to marine ecosystem and environmental changes: Global and Planetary Change, v. 105, p. 121–134. doi:10.1016/j.gloplacha.2012.02.011

Shen, J., Algeo, T.J., Zhou, L., Feng, Q., Yu, J., and Ellwood, B. B., 2012, Volcanic perturbations of the marine environment in South China preceding the latest Permian mass extinction and their biotic effects: Geobiology, v. 10, p. 82–103. doi:10.1111/j.1472-4669.2011.00306.x

Shen, S.-Z., Crowley, J.L., Wang, Y., Bowring, S.A., Erwin, D. H., Henderson, C.M., Ramezani, J., Zhang, H., Shen, Y., Wang, X.-D., Wang, W., Mu, L., Li, W.-Z., Tang, Y.-G., Liu, X.-L., Liu, X.-L., Zeng, Y., Jiang, Y.-F., and Jin, Y.-G., 2011a, High-precision geochronologic dating constrains probable causes of earth's largest mass extinction: Science, v. 334, p. 1367–1372. doi:10.1126/science.1213454

Shen, W., Sun, Y., Lin, Y., Liu, D., and Chai, P., 2011b, Evidence for wildfire in the Meishan section and implications for Permian-Triassic events: Geochimica Et Cosmochimica Acta, v. 75, p. 1992–2006. doi:10.1016/j.gca.2011.01.027

Downloaded by [USGS Libraries] at 12:06 18 February 2015

Son, T.H., Koeberl, C., Ngoc, N.L., and Huyen, D.T., 2007, The Permian-Triassic boundary sections in northern Vietnam (Nhi Tao and Lung Cam sections): Carbon-isotope excursion and elemental variations indicate major anoxic event: Palaeoworld, v. 16, p. 51–66. doi:10.1016/j.palwor.2007.05.010

Song, H., Tong, J., Chen, Z.Q., Yang, H., and Wang, Y., 2009, End-Permian mass extinction of foraminifers in the Nanpanjiang Basin, South China: Journal of Paleontology, v. 83, p. 718–738. doi:10.1666/08-175.1

Song, H., Wignall, P.B., Tong, J., and Yin, H., 2013, Two pulses of extinction during the Permian–Triassic crisis: Nature Geoscience, v. 6, p. 52–56.

Thomas, B.M., Willink, R.J., Grice, K., Twitchett, R.J., Purcell, R.R., Archbold, N.W., George, A.D., Tye, S., Alexander, R., Foster, C.B., and Barber, C.J., 2004, Unique marine Permian-Triassic boundary section from western Australia: Australian Journal of Earth Sciences, v. 51, p. 423–430. doi:10.1111/j.1400-0952.2004.01066.x

Thomson, D.J., 1982, Spectrum estimation and harmonic analysis: Proceedings of the IEEE, v. 70, p. 1055–1096. doi:10.1109/PROC.1982.12433

Vinn, O., 2010, Shell structure of helically coiled microconchids from the Middle Triassic (Anisian) of Germany: Paläontologische Zeitschrift, v. 84, p. 495–499. doi:10.1007/s12542-010-0064-y

Wang, Y., and Henderson, C., 2003, Report of the workshop "Lopingian stratigraphy and events": Permophiles, no. 43, p. 5–7.

Weidlich, O., Kiessling, W., and Flügel, E., 2003, Permian-Triassic boundary interval as a model for forcing marine ecosystem collapse by long-term atmospheric oxygen drop: Geology, v. 31, p. 961–964. doi:10.1130/G19891.1

Wignall, P.B., and Twitchett, R.J., 1996, Oceanic anoxia and the end Permian mass extinction: Science, v. 272, p. 1155–1158. doi:10.1126/science.272.5265.1155

Wu, Y.S., Jiang, H.X., and Fan, J.S., 2010, Evidence for sea-level falls in the Permian-Triassic transition in the Ziyun area, South China: Geological Journal, v. 45, p. 170–185.

Yin, H., Zhang, K., Tong, J., Yang, Z., and Wu, S., 2001, The global stratotype section and point (GSSP) of the Permian–Triassic boundary: Episodes, v. 24, p. 102–114.

Zhang, K.X., Tong, J.N., Shi, G.R., Lai, X.L., Yu, J.X., He, W.H., Peng, Y.Q., and Jin, Y.L., 2007, Early Triassic conodont-palynological biostratigraphy of the Meishan D Section in Changxing, Zhejiang Province, South China: Palaeogeography, Palaeoclimatology, Palaeoecology, v. 252, p. 4–23. doi:10.1016/j.palaeo.2006.11.031

Downloaded by [USGS Libraries] at 12:06 18 February 2015